

The June 2013 Alberta Catastrophic Flooding Event – Part 2:

Fine-scale precipitation and associated features

B. Kochtubajda¹, R.E. Stewart², S. Boodoo³, J. M. Thériault⁴, Y. Li⁵,

A. Liu¹, C. Mooney¹, R. Goodson¹ and K. Szeto⁶,

¹Environment and Climate Change Canada, Edmonton, AB, Canada

²University of Manitoba, Winnipeg, MB, Canada

³Environment and Climate Change Canada, King City, ON, Canada

⁴Université du Québec à Montréal, Montréal, QC, Canada

⁵Global Institute for Water Security, University of Saskatchewan, Saskatoon, SK, Canada

⁶Environment and Climate Change Canada, Toronto, ON, Canada

Manuscript submitted to the 2013 Alberta Flood Special Issue in Hydrological Processes

Version: September 25, 2015

Revised manuscript : March 3, 2016

Corresponding author: Bohdan Kochtubajda, Meteorological Service of Canada, Environment and Climate Change Canada, 9250 – 49th Street NW, Edmonton (Alberta) T6B 1K5

Email: bob.kochtubajda@canada.ca

ABSTRACT

Data obtained from a variety of sources including, the Canadian Lightning Detection Network, weather radars, weather stations and operational numerical weather model analyses were used to address the evolution of precipitation during the June 2013 southern Alberta flood. The event was linked to a mid-level closed low pressure system to the west of the region and a surface low pressure region initially to its south. This configuration brought warm, moist unstable air into the region that led to dramatic, organized convection with an abundance of lightning and some hail. Such conditions occurred in the southern parts of the region whereas the northern parts were devoid of lightning. Initially, precipitation rates were high (extreme 15-min rainfall rates up to 102 mm h^{-1} were measured) but decreased to lower values as the precipitation shifted to long-lived stratiform conditions. Both the convective and stratiform precipitation components were affected by the topography. Similar flooding events, such as June 2002, have occurred over this region although the 2002 event was colder and precipitation was not associated with substantial convection over southwest Alberta.

Keywords: Alberta flooding, orographic precipitation, convection, upslope flow, radar, lightning

1. INTRODUCTION

Heavy precipitation and associated flooding is a critical issue in many regions of the world. The severity of rainstorms and their associated impacts is dependent on several characteristics including total rainfall amount, peak rainfall intensity, storm duration, and whether the precipitation is convective or stratiform in nature (Trenberth et al., 2003; Raddatz and Hanesiak, 2008). The Fifth Assessment Report of the Intergovernmental Panel on Climate Change furthermore concluded that heavy precipitation events in some regions have increased since 1950 (IPCC, 2014).

Past studies of Alberta rainstorms resulting in major large-scale flooding have shown complex interactions between atmospheric and hydrological processes and the Rocky Mountains (Reuter and Nguyen, 1993; Ou, 2008; Szeto et al., 2011; Pennelly et al., 2014; Shook, 2015). Recent model simulations of rainstorms in 2005 (Flesch and Reuter, 2012) found that the Rocky Mountains affected precipitation amounts in the mountains and foothills due to orographic lifting and that the mountains may prolong the duration of these rainstorms.

An intense weather system in June 2013 triggered severe flooding over numerous communities in southern Alberta, left five fatalities, displaced more than 100,000 people, and caused substantial damage to the regional road and bridge infrastructure (Pomeroy et al., 2015). This event became the costliest natural disaster in Canadian history (\$6 billion) and was identified as the top Canadian weather event that year (Phillips, 2014). In Part 1, Liu et al. (2016, this volume) investigated the antecedent and large scale processes leading to the June 2013 Alberta flooding. The synoptic scale features were not particularly intense when compared to other cut-off low cases. However, the 2013 storm environment was the most convectively unstable amongst the 23 long-lived precipitation events in the lee of the Rocky Mountains of southern Alberta investigated by Szeto et al. (2016). Simulation of this event (Li et al., 2016) illustrated the evolution of precipitation during the convective phase.

Thunderstorms are an important component of the global water cycle, because they represent one of the mechanisms responsible for cycling moisture (Llasat and Puiggervet, 1997; Changnon, 2001). Varying amounts of rainfall, hail and lightning associated with thunderstorms can be produced in flooding events. Some thunderstorms can generate intense rainfall over short

periods of time, often triggering flash floods (Soula et al., 1998, Llasat et al., 2010). Alternatively, a slow moving thunderstorm complex around Vanguard, Saskatchewan on July 3, 2000 produced copious lightning and the largest recorded 8-h precipitation event (up to 375 mm) on the Canadian Prairies and inundated homes, farms and surrounding roads and rail lines (Hunter et al., 2002). Thunderstorms also contributed to the August 2002 central European floods (Ulbrich et al., 2003) and the June 2008 floods in Iowa (Smith et al., 2013). Lightning analyses of two intense rainfall periods in the vicinity of Boulder during the September 11-13, 2013 Great Colorado Flood identified a low number of very high frequency radiation sources emitted by lightning discharges during the first period and no lightning activity in the second period (Friedrich et al., 2015). Few studies, however, have quantified the fraction of thunderstorm rainfall contributing to large flooding events. During the 1993 “great flood” over the Upper Mississippi River Basin the relationship between cloud-to-ground lightning and the associated rain volume was examined and found to be useful in estimating the locations and amounts of convective rainfall (Kempf and Krider, 2003).

The objective of this study is to expand on the analysis of the 2013 event (Liu et al., 2016) by examining the evolution of the precipitation from the initial convective phase and subsequently transitioning to the stratiform phase. Several questions are addressed including:

What fraction of the total precipitation was contributed by thunderstorm processes? How did the convective and stratiform processes evolve spatially and temporally? How did the radar-derived rainfall rates and accumulations compare to the rain gauge measurements? How did topography influence the evolution of rainfall intensity?

2. DATA AND METHODOLOGY

A variety of observational and operational datasets and research model products are utilized in this study. Observations include radar information, ground-based GPS sensing equipment, surface weather stations, and lightning network information. Other products include operational Canadian numerical weather model information. Some of these datasets have been described in Liu et al. (2016).

2.1 Radar

Environment Canada's (EC) operational radar network (Joe and Lapczak, 2002) provided radar images for the storm event. Reflectivity composites of constant altitude plan position indicator (CAPPI) scans, which can be used to infer precipitation intensity at a specified altitude (in this case at 1.5 km above ground level), were derived from volumetric scans from the Carvel (WHK) radar near Edmonton, Strathmore (XSM) near Calgary, Schuler (XBU) near Medicine Hat in Alberta, and Silver Star Mountain (XSS) near Kelowna in British Columbia. These data have a spatial resolution of 1 km by 1° in azimuth with a maximum range of 250 km. Doppler scanning at 0.5°, 1.5° and 3.5° elevations provides clutter-filtered reflectivity and radial velocity information at 0.5 km by 0.5° resolution extending to 112 km. The scans are repeated every 10 minutes. Data processing was performed by the **CANadian Radar Decision Support (CARDS)** system (Joe et al., 2003).

Vertical reflectivity profile and precipitation rate analyses of radar echoes detected from XSM were performed over three surface observation sites; at the Calgary West Cr10 Auto (CWS), Burns Creek (BCR), and Kananaskis Boundary Auto (KAN) stations. Their elevations and distances from the radar are listed in Table 1, along with the height of the radar beam above each station for the 0.5° elevation scan. Vertical reflectivity profiles were derived from the 24 elevation volume scans to indicate the evolution of precipitation over these locations. Radar-derived precipitation rates at 10-min intervals were determined from the reflectivity data at the lowest elevation scans using the operational standard Marshall-Palmer reflectivity to rain-rate (Z-R) relation. Since BCR and KAN are outside the maximum Doppler range for XSM, only the spatially coarser reflectivities from the lowest elevation in the volume scans were used. Additionally, the Doppler scans provided an estimate of the mean radial wind field (VAD) with height as a function of time throughout the event.

2.2 Lightning and precipitation

Lightning data combined with gauge-measured rainfall can be used to differentiate convective / stratiform precipitation regimes. Lightning and precipitation data were obtained from the Canadian Lightning Detection Network (CLDN) and the archives of Environment Canada and

the AgroClimatic Information Service (ACIS) of Alberta Agriculture and Rural Development, respectively. The CLDN, established in 1998, is operated by Environment Canada. This network has undergone several sensor upgrades (Burrows and Kochtubajda, 2010), and currently consists of 83 Enhanced Lightning Sensors (LS7000 and LS7001). These sensors detect and locate low frequency (LF) electromagnetic signals generated by cloud and cloud-to-ground (CG) lightning discharges using direction finding and time-of-arrival methodologies described in Cummins and Murphy (2009). In addition to the time and location, CLDN flash data provide information on the peak current from the first return stroke of each flash, the number of strokes per flash and the polarity. The typical charge structure of an isolated, mature thunderstorm consists of positive charge in the upper levels and negative charge in lower levels. However, the structure can be complicated depending on the storm type, cloud type, geographic location, and stage of development (Stolzenburg and Marshall, 2008). The polarity (negative or positive) of a CG flash reflects the cloud charge source region of the thunderstorm where the flash originates. Median location accuracies of CG lightning flashes are about 500 m or better according to Cummins and Murphy (2009). The detection efficiency, as determined by Vaisala Inc., is 80-90% or higher inside the CLDN, decreasing to about 70% just beyond the periphery and to about 30% at 300 km beyond the network.

Between the two sources of surface weather information, 43 precipitation stations within the Bow and Oldman River sub-basins were examined (Figure 1). A database of hourly precipitation and lightning observations was prepared for each station. A station was deemed to experience ‘thunderstorm rain’ when coincident lightning and rainfall occurred within a 1 h period and within 20 km range of each station. Rainfall from such periods was accumulated to derive a total thunderstorm rain amount.

2.3 Numerical weather model output

Meteorological forecasts produced by the limited area model (LAM) version of the Global Environmental Multiscale (GEM) model (otherwise referred to as the GEM-LAM) over western Canada were used to support the observational analysis of the flooding event. The GEM-LAM model is described in Mailhot et al. (2014). Condensation processes, described in Milbrandt and Yau (2005), predict the total concentration and the mass mixing ratio of cloud droplets, rain, ice

crystals, snow, graupel and hail. These fields, along with temperature and vertical motion, were analyzed using the forecast produced at 1800 UTC 19 June 2013.

3. PRECIPITATION, LIGHTNING AND THUNDERSTORMS

The weather over southern Alberta surrounding the 2013 heavy rain event was quite unstable and numerous severe thunderstorms, rainfall and tornado warnings were issued from June 17-22. Lightning activity was frequent and reflected a diurnal trend (Liu et al. 2016, Figure 7c). A review of regional severe weather events showed reports of funnel clouds, tornadoes and large hail (Cummine, 2014). For example, areas east of Lethbridge reported golfball-sized hail, and a tornado touched down near Pakowki Lake (located 146 km southeast of Lethbridge) in the mid-afternoon and early evening of June 19.

Unlike the June 2002 storm (Szeto et al., 2011) or the July 2005 storms over southern Alberta (Ou, 2008) which generated little lightning, the 2013 event produced an abundance of lightning and associated thunderstorms that contributed substantially to the rainfall accumulation. As an example, Figure 2a illustrates the precipitation and lightning activity from June 17-22 at the BCR station located in the Bow sub-basin. A few scattered showers between June 17 (1200 UTC) and June 19 (0600 UTC) produced approximately 16 mm of rainfall. On June 19, convection produced varying amounts of lightning and rainfall from early evening to midnight. The first CG flashes occurred on June 20 at 0024 UTC and lightning activity ceased several hours later (June 20 at 0510 UTC). A total of 129 CGs were detected of which the majority was of negative polarity (63%). Hourly flash and rainfall rates of 49 fl h^{-1} and 23 mm h^{-1} , respectively, were measured during the peak of the thunderstorm event. Two negative CG flashes were detected at 0713 UTC. Rainfall rates then decreased to lower values as the precipitation shifted to long-lived stratiform conditions. Thunderstorm rainfall associated with the lightning accounted for approximately 35% of the 343 mm of rainfall measured at BCR from 1500 UTC June 19 to 2300 UTC June 21.

Lightning activity over the remaining stations in the Bow sub-basin exhibited similar temporal tendencies. The first CG flashes were detected between June 19 at 2330 UTC and June 20 at

0330 UTC and ended three to six hours later. Maximum hourly flash rates and rainfall rates measured at these stations varied from 1 to 92 fl h⁻¹ (median 16 fl h⁻¹) and from 3 to 30 mm h⁻¹ (median 12.3 mm h⁻¹) respectively. Positive polarity flashes, which accounted for 21-68% of the lightning activity over the stations, were anomalously high. Typically, positive flashes comprise about 12% of CG lightning activity in western Canada during the summer months (Kochtubajda and Burrows, 2010). Several situations have been identified that favor more frequent occurrences of positive lightning, including the dissipating stages of thunderstorms and the mature and later stages of some severe storms (Rakov and Uman, 2003). A temporal analysis of the lightning activity revealed that the peak +CG activity typically occurred during the dissipating stages of the thunderstorms at most of the stations. From a hydrological perspective, precipitation rates become lighter during the decaying stages. Consequently, the high fraction of positive CGs may be indicative of the evolution from convective to stratiform precipitation. However, at some stations the peak positive activity was observed during the mature stage.

Rainfall amounts associated with the thunderstorms over the weather stations in the Bow sub-basin varied from 3 mm to 122 mm, and contributed between 3% and 55% of the total rainfall (Figure 3a). Extreme 15-min rainfall rates up to 87 mm h⁻¹, indicative of intense downpours, were measured at some locations. A gradient in thunderstorm rain at the northern edge is evident when the fractional thunderstorm contributions at the BCR and KAN stations (a distance of 39 km) are compared. Although the total rainfall measured at each gauge was similar, thunderstorm rainfall accounted for 35.4%, and 15.7% of the total amount, respectively.

Thunderstorms over the weather stations in the Oldman sub-basin produced similar rainfall amounts ranging from 8.8 mm to 112 mm (Figure 3b). However, the fractional contributions to the total rainfall as well as rainfall rates and lightning activity were markedly different from those stations located in the Bow sub-basin. Maximum hourly flash rates were more intense over these stations varying from 40 fl h⁻¹ and 159 fl h⁻¹ (median 78 fl h⁻¹). Maximum hourly rainfall rates varied from 7 mm h⁻¹ and 47 mm h⁻¹ (median 21.4 mm h⁻¹). Positive polarity flashes accounted for 6-54% of the lightning activity. Extreme 15-min rainfall rates up to 102 mm h⁻¹ were measured at some locations and thunderstorm rainfall contributions varied between 20% and 84% of the total rainfall.

The scatterplot in Figure 4 shows a positive relationship between increased lightning activity and increased thunderstorm contributions to the total rainfall. The Spearman rank correlation computed for the data is 0.78 (significant at the 1% level). Additionally, we note a difference in thunderstorm contributions when lightning events exceed 100 CG flashes. Specifically, thunderstorm rainfall accounted for an average of 20.8% (varying from 3% -55%) of the total rainfall at stations where < 100 CG flashes were detected and 49% (varying from 23% to 84%) when > 100 CGs were detected

4. PRECIPITATION FEATURES

4.1 Evolving radar patterns

The temporal evolution of radar reflectivity patterns illustrating the evolving character of precipitation during the event is shown by CAPPI images in Figure 5. Convective cells were moving northeastwards across the foothills of southern Alberta starting on June 19. Later in the day the individual cells started to organize into an intense convective line oriented northwest to southeast. Figure 5a shows the convective lines at 0300 UTC on June 20th 2013, with the upper section of the line more or less parallel to the foothills, over the KAN and BCR sites. At these locations the storm cells were small with core reflectivities of about 45 dBZ. Farther to the southeast, a more intense line with maximum core reflectivity of about 60 dBZ was approaching YXH, while north of XBU an intense west-east oriented line of storms had developed. As the system progressed, the convective cells organized into larger lines of thunderstorms extending over larger areas of southern Alberta. Figure 5b shows the CAPPI composite at 0500 UTC. The line of thunderstorms approached the Calgary Airport (YYC) and the XSM radar from the southwest on the lee of the Rockies, and reflectivity was in the 50-55 dBZ range along the leading edge. Another more intense convective line approached Medicine Hat Airport (YXH) and the XBU radar farther southeast, and moved with the same general flow from the southwest. Reflectivities along this line exceeded 55 dBZ, and were close to 60 dBZ in individual cores. The line of storm clusters over YXH (south of XBU) moved northward past XBU and approached the cluster of storms to the north. By 0800 UTC, in Figure 5c, the storm lines seemed to merge at the western edge while the high reflectivity cores along the line became weaker. The precipitation over YXH, YYC, KAN and BCR was mostly stratiform. By 1500 UTC June 20, (Figure 5d),

almost all of the convective elements had dissipated, and rainfall over XSM was largely stratiform and by 2100 UTC (Figure 5e), there was only light rain over KAN and BCR.

The mean radial wind field obtained from the 3.5° Doppler scan from XSM is presented in Figure 6. It displays the mean wind speed and direction within 112 km as a function of height and time during the heavy precipitation period from 0000 UTC June 19 to 0000 UTC June 22. At about 0500 UTC June 19, the VAD winds at the upper levels (3-8 km AGL), showed very little directional change and were on average from the southwest. The estimated mean wind was around 10 m s⁻¹ and approached 15 m s⁻¹ between 4 and 5 km. Below 2.0 km, the wind speed remained low (< 5 m s⁻¹), but its direction was on average from the southeast. From about 0900 UTC June 19 to 0000 UTC June 20, the VAD winds began showing a directional shift, from southeast to east as the low level wind speed increased. The winds remained relatively easterly, and intensified during the period of heavy rainfall from about 0000 UTC to 2000 UTC June 20th. The average wind speed above 2.0 km during this period was approximately 20 m s⁻¹. Below 2.0 km, there was strong shear indicating the presence of a low level jet with speeds up to about 30 m s⁻¹.

4.2 Radar observations at selected locations

4.2.1 Time series of vertical reflectivity profiles over BCR, CWS and KAN stations

The BCR, CWS and KAN surface sites were selected to explore the temporal characteristics of the radar echoes. BCR is located 123 km from XSM along radar azimuth 238°, whereas CWS and KAN are 44 km and 124 km away respectively, but along the 256° azimuth. Reflectivity fields were averaged along a vertical column over each of the sites from the 10-min volume scans for the duration of the event to produce an averaged vertical reflectivity profile. Figure 2a shows the averaged vertical reflectivity profiles (VRP) at BCR. The radar beam is ~1.5 km relative to the radar height and since BCR is about 900 m higher in elevation than XSM, the lowest scan is effectively 600 m above the station. The radar beam is also very wide at this distance and the reflectivity measurements over BCR are prone to ground clutter contamination. However, during moderate to heavy precipitation the returns from the ground clutter were

overshadowed by the precipitation returns. Short rainfall periods over BCR occurred around 1200 UTC to 2000 UTC on June 18 and also from 0200 UTC to 0800 UTC on June 19 2013. An extended period of precipitation, from about 0000 UTC June 20 2013 through June 22 2013, led to the largest contribution of rainfall over this site for the event. During the heaviest rainfall period (about 0100 UTC to about 0800 UTC on June 20 2013), deep convection produced CG lightning with average flash rates of 20 fl h^{-1} (Figure 2a upper panel). At about 0200 UTC the flash rates peaked to about 50 fl h^{-1} . The precipitation profiles were mostly convective initially with mean reflectivities at the lowest elevation exceeding 40 dBZ and the depth of the mean reflectivity profiles were close to 10 km. The rainfall period from 0100 UTC to 1600 UTC contributed most to the total accumulation over the site. The hourly averaged gauge rainfall rates (solid line) were not excessively high; the peak rate was almost 25 mm h^{-1} at 0200 UTC on June 20 which then subsequently varied between 10 and 20 mm h^{-1} during the convective rainfall. For the rest of the event the hourly averaged gauge rain rates were on the order of 5 mm h^{-1} . The rain-gauge accumulated rainfall (dotted line in the lower panel) was initially about 50 mm and increased to 250 mm, in approximately 15 hours. Rain continued over the site for several hours until about 0000 UTC on June 22 at which time the gauge estimate was about 360 mm total accumulation.

CG lightning flashes in the upper panel and VRP in the lower panel are shown in Figure 2b for the CWS station. The lowest radar scan from XSM was about 350 meters above CWS and provided a more complete picture of the reflectivity profiles. Storm cells passing over the site had reflectivity profiles extending to almost 10 km and were associated with lightning during the initial rainfall period. The maximum flash rate occurred at 1600 UTC on June 18 with values exceeding 60 fl h^{-1} . Lower flash rates (10 to 20 fl h^{-1}) were observed for shorter periods at 0700 UTC June 19 and from 0400 UTC to 0700 UTC on June 20. During the convective period from about 1400 UTC June 18 to 0700 UTC June 20 the gauge recorded rainfall was only about 15 mm. Rainfall over CWS became more stratiform from 0700 UTC June 20 to 1700 UTC June 20 and the radar bright band (melting layer) was clearly visible in the reflectivity profiles. In the melting layer, the reflectivity peaked at 40 dBZ and then decreased to about 30 dBZ below. From 1400 UTC June 20 to 1600 UTC June 20 the reflectivities at the lowest level were close to 40 dBZ. There was also a slight lowering of the melting layer during this period. For the rest of the

event, the rainfall over the site became more sporadic with occasional bursts of rainfall and by the end of the event the gauge recorded 78.3 mm total precipitation at this location.

The KAN site is located about 39 km north of BCR along the foothills of the Rockies. It is along the same 256° radial as CWS and about the same distance to XSM as BCR. The height of radar beam over KAN was about 1.1 km above the ground level as KAN is lower in altitude than BCR. The VRPs were not affected by ground clutter but the radar only captured the portions of the VRP that were above the melting layer. Some convective elements in the reflectivity profiles were detected, for example the deep echo top at 8.0 km at 0200 UTC June 20. The lightning flash rates in the upper panel in Figure 2c show low lightning activity relative to BCR and CWS, with flash rates $< 5 \text{ fl h}^{-1}$. From 0100 UTC to about 0800 UTC on June 20 the rainfall over KAN was mostly convective and then transitioned into stratiform rainfall. The hourly averaged gauge rainfall rate (solid line) was on the order of 10 to 15 mm h^{-1} . During a 17 hour period, the rain-gauge recorded an increase of 190 mm rainfall from 10 mm at 0100 UTC June 20 to 200 mm at 1800 UTC June 20. The resulting rain gauge rainfall ending at 0000 UTC June 22 was 290 mm.

4.2.2 Vertical radar cross-section over Burns Creek

Burns Creek recorded the largest gauge-recorded total rainfall accumulation of the three stations presented above. Figure 7 shows selected vertical cross-sections of reflectivity over BCR from 0130 UTC to 0500 UTC on June 20 at 30 minute intervals from the Strathmore radar. At 0130 UTC, Figure 7a, the storm cell was over BCR (123 km range) and the radar echo showed deep convection with the echo top extending to well above 10 km. The cell consisted of two strong reflectivity cores which extended about 20 km along the radial and shows a small area of greater than 50 dBZ, just a few kilometers from BCR. In Figures 7b to 7f from 0200 UTC to 0400 UTC, several convective cells closer to the radar (less than 70 km) are seen, with high reflectivity regions extending horizontally from 10 to 20 km along the radial. The echo tops were about 10 km and reflectivities greater than 50 dBZ were present in the downdraft regions. The westward tilt of radar reflectivities from an elevation of approximately 5 km down towards the surface is especially noticeable in Figures 7c and 7d. Raindrop fall speeds near the surface vary from approximately 4 to 9 m s^{-1} (Gunn and Kinzer, 1949). It is believed that the tilt was a result of

raindrops falling through continual easterly winds down to the surface in which the strongest values (approaching 30 m s^{-1}) were below 2 km as shown between 0000 to 2000 UTC June 20 from the VAD analysis (Figure 6). Such a sheared environment affects the trajectory of precipitation particles as first discussed by Marshall (1953), and in this case the trajectories tilt to the west as they approach the surface. At 0400 UTC in Figure 7f, a deep convective cell extending between the 60 and 70 km range shows a reflectivity core exceeding 55 dBZ, possibly indicating hail or melting graupel at about 2.0 km. In Figures 7g (0430 UTC) and 10h (0500 UTC), the cross-sections still indicated some embedded convection within a more widespread stratiform pattern as the melting layer became more prominent.

4.3 Transition from convective to stratiform precipitation

The occurrence of precipitation types at BCR, the vertical motion fields and variation of the freezing level have been analyzed using the GEM-LAM to investigate the weather conditions during the transition from convective to stratiform precipitation

Mostly liquid precipitation occurred on 20 June (Figure 8). The freezing level (0°C line) was located just below 4 km ASL until 0600 UTC, then it decreased slightly to 3.5 km, and subsequently increased again at later times. Note that the model ground level at BCR is 2.17 km. A 2 km deep melting layer allowed all solid precipitation (graupel) to melt completely into rain before reaching the surface. Graupel was produced between 0200 and 0500 UTC, during the convective precipitation production at high elevation (9 km ASL). The deep cloud formed during the convective period producing ice crystals that grew into snowflakes. These ice particles collected cloud liquid drops to produce graupel. The strong upward air motion produced at that time resulted in supersaturation conditions mainly at heights above 5 km.

Observations suggest that the transition from convective to stratiform precipitation occurred between 0700 and 0800 UTC, which is also supported by the GEM-LAM forecast. Figure 9 shows the vertical motion cross-section field from the radar looking towards Burns Creek at 0400 UTC, during the convective precipitation period, and at 0800 UTC, which is just after the

beginning of the stratiform precipitation. It shows that strong upward motion occurred near Burns Creek as well as upstream of the mountainside. The depth of the strong upward motion corresponds to the location where graupel was predicted to form above Burns Creek (Figure 8). The tilted vertical motion pattern above the ridge top suggests a combination of orographic forcing and vertical wind shear. On the other hand, much weaker and broad vertical motion is produced at 0800 UTC, which is associated with the onset of the stratiform precipitation period. The minimum value of vertical motion is less than at 0400 UTC and is mainly orographically forced.

At 0800 UTC 20 June, the freezing level started to descend towards the surface southwest of Burns Creek. The decrease in the elevation of the freezing level could change the type of precipitation reaching the surface by affecting the melting rate of the solid precipitation falling through the melting layer. The variation of the freezing level with respect to surface elevation over the area of interest is depicted in Figure 10. It shows that the freezing level was well above ground (> 3 km) in the foothills and towards eastern Alberta during the storm (0200-1200 UTC). However, the freezing level southwest of BCR is very close to the ground at 0600 UTC (Figures 10 c and d) during the transition from convective to stratiform precipitation. It increased again after 0800 UTC. This variation in the freezing level suggests that liquid precipitation reached the ground during most of the storm east of the mountains. On the other hand, solid precipitation may have reached the ground in the mountains, which would have affected the severity of the flooding event by decreasing the rain-on-snow occurrence for at least a few hours.

4.4 Radar accumulation patterns

Radar-derived rain accumulations from XSM and XBU are shown in Figure 11 from 0000 UTC June 18 to 2350 UTC June 22, 2013. As mentioned earlier, the event consisted of localized severe convective storms initially, producing large hail and intense rainfall, followed by widespread stratiform rainfall. XSM captured the bulk of the precipitation for the event and most of the accumulation was to the southwest of the radar. The highest accumulation was in the foothills between 80 and 120 km southwest of XSM with accumulation greater than 200 mm over a large area. There were also pockets with > 250 mm accumulation inside this area. The higher

radar amounts may have been contaminated by ground clutter from the hills in the area. At the Calgary Airport (YYC), ~40 km from XSM, the radar estimated about 100 mm total rainfall accumulation. At KAN and BCR the amounts were about 120 and 240 mm respectively. Another heavy accumulation band extended from the foothills southeastward towards the Lethbridge Airport (YQL), roughly 160 km south-southeast of XSM and was also seen by XBU. At 130 km southwest of XBU, the smaller area of heavy localized accumulation show amounts exceeding 200 mm, as a result of the convective storms. At Medicine Hat Airport (YXH) (42 km southwest of XBU), radar-estimated rainfall was 30-40 mm. Areas to the north of XBU, experienced more widespread accumulation amounts (>100 mm in some parts), and up to 200 mm in the convective cores embedded in the stratiform regions.

4.4.1 Time series comparison of radar-derived and gauge-measured rainfall rates and accumulation at BCR, CWS and KAN

The derived rates were compared to the hourly-averaged gauge rainfall rates and accumulations and presented in Figure 12 at BCR, CWS and KAN. The upper panels in Figure 12 show the radar derived rates (thin line) and the hourly-averaged rain gauge rates (thick line). In Figure 12a, over BCR, from 1000 UTC June 18 to about 0300 UTC June 20, the radar derived rates were higher overall, with peak rates at about 15 mm h^{-1} . The hourly averaged gauge rates were about 5 mm h^{-1} . The long temporal averaging of the gauge rates reduces the peaks within the averaging period compared to the radar-derived rates. From 0300 UTC June 20 to 0100 UTC June 22, the hourly averaged gauge rates were higher than the radar estimated rates, with a peak gauge rate of 23 mm h^{-1} at 0300 UTC June 20 and falling to about 5 mm h^{-1} by 2200 UTC. Rainfall rates remained relatively low on average for the rest of the event. The lower panel in Figure 12a shows the cumulative accumulation or rainfall from the radar estimate (dashed line) and the gauge amount (dotted line). At about 0300 UTC June 20 the radar accumulation was 80 mm and the gauge was 50% lower. However, from this time onwards the gauge accumulation was higher and resulted in 360 mm total rainfall compared to about 240 mm estimated from the radar. The lower radar estimated rates and accumulations at BCR are partly due to its distance from the radar (123 km), i.e. the radar beam is sampling the upper levels of the precipitation

system, thereby missing the higher reflectivities closer to the ground and also because of signal attenuation.

Figure 12b shows similar plots, but for the CWS location. Note that because CWS is much closer to the radar (44 km), the radar's sampling volume is much smaller and the beam is much closer in height to the rain-gauge than at BCR. The upper panel (Figure 12b) shows that both radar-estimated and gauge-measured rates were relatively the same and mostly below 10 mm h^{-1} , although higher radar-derived rainfall rates during the convective periods were evident. Both radar and gauge accumulations follow each other very closely over the entire rainfall period (Figure 12b lower panel) and resulted in 80 mm accumulation at the station.

At KAN, the upper panel in Figure 12c, peak radar rates were about 15 mm h^{-1} during the convective episodes on June 19 and early June 20. The hourly averaged gauge rates after 0300 UTC June 20 ranged from 10 to 18 mm h^{-1} while the radar derived rates were relatively low at 5 mm h^{-1} . The gauge accumulation, solid line lower panel, in Figure 12c resulted in 290 mm total accumulation whereas the radar derived total (dashed line) was about 60% lower. The radar sampling characteristics at KAN was similar to BCR, its distance from the radar and being similarly affected by attenuation during heavy precipitation periods produced rates and accumulation much lower than the gauge estimates.

4.5 Influence of topography

The study area encompasses mountainous regions (2-3 km ASL), foothills regions (1-2 km ASL) and the plains region (0.6-1 km ASL). Precipitation gauges within the Bow and Oldman catchment areas were positioned at a variety of elevations. As illustrated in Figure 13, it is apparent that precipitation amounts for the event depended somewhat on gauge elevation as well as spatial location. Lowest amounts were recorded at the lowest elevations; highest amounts were linked with high elevations; but lower amounts also occurred at high elevations. Overall, these results suggest association with elevation, although this was not the only factor. This has important hydrological implications because runoff is more efficient over sloping terrain which may increase the risk of downstream flooding (Pomeroy et al., 2015).

To examine topographic influences in more detail, the evolution of rainfall intensity and CG flash activity as a function of elevation is summarized in 6-hrly time intervals from 07 UTC June 19 to 06 UTC Jun 22 (Figure 14). Stations measured no rain or very light rain during the period from 07-18 UTC Jun 19 at all elevations (Figure 14a) and occasional dry lightning episodes at some stations in the foothills and plains regions (Figure 14b) were detected. Median rain rates in the mountainous, foothills and plains regions were $< 0.2 \text{ mm h}^{-1}$. Over the next 6 hours, median rain rates intensified at several locations in the mountainous and foothills regions, as CG flashes from thunderstorm cells were first detected between 23 UTC June 19 and 00 UTC June 20.

Moderate to heavy rain rates associated with thunderstorm cells discharging CG flashes were dominant at all elevations during the period of 01 – 06 UTC June 20 (Figures 14 c, d). Median rain rates were 10.1 mm h^{-1} , 6.7 mm h^{-1} and 3.5 mm h^{-1} in the mountainous, foothills and plains regions, respectively. Rain rates from embedded cells subsequently weakened at elevations $> 1800 \text{ m}$ to a median value of 3.8 mm h^{-1} during the period 07 – 18 UTC June 20 as the transition to stratiform conditions occurred. However, during this period rain rates intensified to 8.1 mm h^{-1} at lower elevations between 1500 and 1800 m ASL. Rain rates at elevations between 1200 and 1500 m ASL intensified during the period 07 – 12 UTC June 20 (median rate of 7.7 mm h^{-1}) and weakened during the period 12 – 18 UTC June 20. This 18-h period accounted for the majority of the precipitation measured at each station. Figures 14 (e-f), illustrate sporadic CG activity from isolated cells and a dissipating system as rain rates became lighter at all elevations.

Our observations indicate that, after the thunderstorm event, less rain with weaker rain rates over higher elevations ($>1800\text{m ASL}$) occurred for the majority of 6-h intervals, consistent with the findings reported on the Colorado storm of September 2013 (Friedrich et al., 2015).

5. CONCLUSIONS

The June 19-21, 2013 precipitation event and subsequent flooding was associated with a major storm system that has been examined from several perspectives and at several scales. Our study

has revealed a number of important aspects of the storm and its associated precipitation, as summarized below.

- The event was characterized by a complex evolution of precipitating features including the initial development of organized and unorganized convection, eventual transition to stratiform precipitation, and strong interaction (and enhancement) with topography.
- Vertical radar data illustrated that precipitating structures over the foothills were typically tilted towards the west. This is consistent with the strongest winds being at low levels and directed to the west according to the radar VAD analyses.
- Precipitation rates were not exceptional with maximum hourly values of 50 mm h^{-1} and extreme 15-min values up to 102 mm h^{-1} . Such values pale in comparison with records reported elsewhere on the Prairies.
- Precipitation illustrated some elevation dependence. During some periods, less rain fell at lower rates over higher elevations than experienced at lower elevations.
- Thunderstorm rainfall contributions varied between 5% and 50% of the total rainfall over stations in the Bow sub-basin, and between 20% and 84% of the total rainfall over stations in the Oldman sub-basin.
- The high fraction of positive lightning flashes may be an indication of the evolution from convective to stratiform precipitation.
- Z-R estimates of rainfall work reasonably well in close proximity to the Strathmore radar. But, distance from the radar and attenuation during heavy precipitation periods led to inferred precipitation rates and accumulations being much lower than gauge estimates over many regions.

In Part 1 of this study, Liu et al. (2016) described the synoptic set-up leading to this precipitation event and the insight from Part 2 can be placed into that context. Liu et al. (2016) showed that the event consisted of two stages - convective and stratiform. The first stage, which lasted 6 to 8 hours, was dominated by convective activity which was characterized by short periods of intense precipitation. The transport of a warm, moist air mass via the easterly low level jet (LLJ) led to a destabilization of the environment which, along with the orographic lift and some upper-level

divergence, provided a favorable environment for convective development. This convection was associated with thunderstorm cells that contributed substantially to rainfall accumulations. From a hydrological perspective, the spatially synchronous timing of peak water levels of the flood peak on the eastern slopes of the Rockies reflected the dominance of the heavy rainfall (Pomeroy et al., 2015).

The transition period from the convective stage to the stratiform stage was rapid (less than 2-3 h) and was associated with an increase in positive CG discharges. An analysis of the Canadian operational weather model also showed that during this period vertical air motions in the foothills became weaker and less cellular in nature.

Above-normal snowfall in the preceding spring helped to maintain a significant snowpack in high-elevation areas before the event. Because the freezing level of the system was relatively high during the early stages, rain rather than snow fell on the still snow-covered mountainous areas. Consequently, while the storage capacity of the thin rocky soils of the headwaters was filled by continuous precipitation within the earlier period of the event, the snowmelt over frozen soils at higher elevations supplemented the precipitation that contributed to downstream flooding (Pomeroy et al., 2015).

The long-lived, stratiform stage was characterized by a synoptic scale low pressure system which provided a continuous supply of moisture through the LLJ, along with an easterly upslope flow and synoptic scale lift which led to continuous precipitation. Precipitation rates during this stage were weaker, but the slowly-evolving nature of the system ensured a long-lived event. In this stratiform stage, an elevation-dependence was noted in which less rain with weaker rain rates occurred over higher elevations (>1800m ASL).

In 2013, there were several extreme flooding events in different parts of the globe, such as the central European flood, and the Great Colorado and southern Alberta floods in North America. In this study, we showed that severe convection and its associated lightning played a significant role in this flooding event, in contrast to the Great Colorado flood of 2013 which exhibited little lightning activity. Several studies have quantified the convective contribution to flash flood events (Soula et al., 1998, Llasat et al., 2010); typically flash floods are associated with isolated

severe thunderstorms. Our analysis quantified the thunderstorm contribution to the total precipitation of a large-scale flooding event.

In summary, this largely atmospheric perspective has illustrated a somewhat typical sequence for such an event although its initial convection was unusual as was its longevity, but its overall precipitation was not. The ensuing flood arose through these and a host of factors at the surface that need to be studied together to understand its devastating features.

ACKNOWLEDGEMENTS

This research is supported by Environment and Climate Change Canada (ECCC) and the Changing Cold Regions Network (CCRN) which is sponsored by the Natural Sciences and Engineering Research Council of Canada (NSERC). Precipitation data were obtained from the National Climate Data and Information Archive of ECCC and the AgroClimatic Information Service, which can be found at <http://www.climate.weatheroffice.ec.gc.ca> and <http://agriculture.alberta.ca/acis/>, respectively. Vaisala Inc. of Tucson, Arizona, USA processes the CLDN data and provides telecommunications services to ECCC. These data are the property of ECCC. The authors would like to acknowledge Katja Winger and Émilie Poirier (UQAM) for providing the GEM outputs. We also thank Alain Pietroniro, Rachel Mintz and Julian Brimelow (ECCC) and the anonymous reviewers for their helpful comments and suggestions.

REFERENCES

- Burrows WR, Kochtubajda B. 2010. A decade of cloud-to-ground lightning in Canada: 1999-2008 Part 1: Flash density and occurrence. *Atmosphere-Ocean* **48**: 177-194. DOI: 10.3137/AO1118.2010
- Changnon SA. 2001. Thunderstorm rainfall in the conterminous United States. *Bulletin of the American Meteorological Society*: **82**: 1925-1940.
- Cummine J. 2014. *2013 Prairie Summer Report: Severe weather event climatology and verification results*. Internal final report. Prairie and Arctic Storm Prediction Centre, Environment Canada, Winnipeg, MB.

Cummins KL, Murphy MJ. 2009. An overview of lightning locating systems: History, techniques and data uses, with an in-depth look at the U.S. NLDN. *IEEE Transactions on Electromagnetic Compatibility*: **51**, 499-518. DOI:10.1109/TEMPC.2009.2023450

Flesch TK, Reuter GW. 2012: WRF model simulation of two Alberta flooding events and the impact of topography. *Journal of Hydrometeorology* **13**: 695-708. DOI:10.1175/JHM-D-11-035

Friedrich K, Kalina E, Aikins J, Gochis D, Rasmussen R. 2015. Precipitation and cloud structures of intense rain during the 2013 Great Colorado Flood. *Journal of Hydrometeorology* DOI:10.1175/JHM-D-14-0157.1, in press.

Gunn R, Kinzer GD. 1949. The terminal velocity of fall for water drops in stagnant air. *Journal of Meteorology* **6**: 243-248.

Hunter FG, Donald DB, Johnson BN, Hyde WD, Hopkinson FW, Hanesiak JM, Kellerhals MOB, Oegema BW. 2002. The Vanguard Torrential Storm (Meteorology and Hydrology), *Canadian Water Resources Journal / Revue canadienne des ressources hydriques* **27-2**: 213-227, DOI: 10.4296/cwrj2702213

IPCC. 2014. *Climate Change 2013: The Physical Science Basis. Contribution of working group I to the Fifth Assessment Report of the Intergovernmental Panel on Climate Change*, Stocker TF, Qin D, Plattner G-K, Tignor M, Allen SK, Boschung J, Nauels A, Xia Y, Bex V, Midgley PM (eds). Cambridge University Press, Cambridge, United Kingdom and New York, NY, USA, 1535 pp.

Joe P, Lapczak S. 2002. Evolution of the Canadian operational radar network. Pages 370-382 in *Proceedings of the Second European Conference on Radar Meteorology (ERAD)*. ERAD Publication Series, vol. 1. Copernicus, Göttingen, Germany.

Joe P, Falla M, Van Rijn P, Stamadianos L, Falla T, Magosse D, Ing L, Dobson J. 2003. *Radar Data Processing for Severe Weather in the National Radar Project of Canada*, 21st Conf. SELS, San-Antonio, TX, AMS, 221-224.

Kempf NM, Krider EP. 2003. Cloud-to-ground lightning and surface rainfall during the great flood of 1993. *Monthly Weather Review* **131**: 140-1149

Kochtubajda B, Burrows B. 2010. A decade of cloud-to-ground lightning in Canada: 1999-2008 Part 2: Polarity, multiplicity and first-stroke peak current. *Atmosphere-Ocean* **48**: 195-209. **DOI:** 10.3137/AO1119.2010

Li Y, Szeto K, Stewart RE, Thériault JM, Chen L, Kochtubajda B, Liu A, Boodoo S, Goodson R, Mooney C. 2016. A numerical study of the June 2013 flood-producing extreme rainstorm over southern Alberta. *Journal of Hydrometeorology*. In review.

Liu A, Mooney C, Szeto K, Thériault JM, Kochtubajda B, Stewart RE, Boodoo S, Goodson R, Li Y, Pomeroy, J. 2016. The June 2013 Alberta Catastrophic Flooding Event: Part 1 – Climatological aspects and hydrometeorological features. *Hydrological Processes*. In review
Llasat MC, Puigcerver, M. 1997. Total rainfall and convective rainfall in Catalonia, Spain. *International Journal of Climatology*: **17**: 1683-1695.

Llasat MC, Llasat-Botija, M, Prat MA, Porcu F, Price C, Mugnai A, Lagouvardos K, Kotroni V, Katsanos D, Michaelides S, Yair Y, Savvidou K, Nicolaidis K. 2010. High-impact floods and flash floods in Mediterranean countries: the FLASH preliminary database. *Advances in Geophysics*, **23**: 47-55.

Marshall JS. 1953. Precipitation trajectories and patterns. *Journal of Meteorology* **10**: 25-29.

Mailhot J, Milbrandt JA, Giguère A, McTaggart-Cowan R, Erfani A, Denis B, Glazier A, Vallée M. 2014. An Experimental High-Resolution Forecast System during the Vancouver 2010 Winter Olympic and Paralympic Games. *Pure and Applied Geophysics* **171**: 209-229

Milbrandt JA, Yau MK. 2005. A Multimoment Bulk Microphysics Parameterization. Part II: A Proposed Three-Moment Closure and Scheme Description. *Journal of Atmospheric Sciences* **62**: 3065–3081. **DOI:** 10.1175/JAS3535.1

Ou AA. 2008. *Meteorological Analysis of Four Rainstorms that Caused Severe Flooding in Alberta during June 2005*. MSc. Thesis Univ. of Alberta, Edmonton, Canada.

Pennelly C, Reuter G, Flesch T. 2014. Verification of the WRF model for simulating heavy precipitation in Alberta. *Atmospheric Research* **135**:172-192.

DOI:10.1016/j.atmosres.2013.09.004

Phillips D. 2014. The top ten weather stories of 2013. *CMOS Bulletin* **42**: 16-24.

Pomeroy JW, Stewart RE and Whitfield PH. 2015. The 2013 flood event in the South Saskatchewan and Elk River basins: causes, assessment and damages. *Canadian Water Resources Journal / Revue canadienne des ressources hydriques*,

DOI: 10.1080/07011784.2015.1089190

Raddatz RL, Hanesiak JM. 2008. Significant summer rainfall in the Canadian Prairie Provinces: Modes and mechanisms, 2000-2004. *International Journal of Climatology* **28**: 1607–1613.

Rakov VA, Uman MA. 2003. *Lightning – Physics and Effects*. Cambridge University Press. Cambridge, United Kingdom. 687pp.

Reuter GW, Nguyen CC. 1993. Organization of cloud and precipitation in an Alberta storm. *Atmospheric Research* **30**: 127-141.

Shook K. 2015. The 2005 flood events in the Saskatchewan River Basin: Causes, assessment and damages. *Canadian Water Resources Journal / Revue canadienne des ressources hydriques*,
DOI: 10.1080/07011784.2014.1001439

Smith, JA, Baeck ML, Villarini G, Wright DB, Krajewski W. 2013. Extreme flood response: The June 2008 flooding in Iowa. *Journal of Hydrometeorology*, **14**: 1810-1825. **DOI:** 10.1175/JHM-D-12-0191.1

Soula S, Sauvageot H, Molinie, G, Mesnard F, Chauzy S. 1998. The CG lightning activity of a storm causing a flash-flood. *Geophysical Research Letters* **25**: 1181–1184. **DOI:** 10.1029/98GL00517

Stolzenburg M, Marshall TC. 2008. Charge structure and dynamics in thunderstorms. *Space Science Reviews*, **137**: 355-272. DOI 10.1007/s11214-008-9338-z

Szeto K, Evans F, Gysbers P. 2016. Long-lived extreme rainstorms in southern Alberta. *Hydrological Processes*, in review.

Szeto K, Henson W, Stewart RE, Gascon G. 2011. The catastrophic June 2002 rainstorm. *Atmosphere-Ocean* **49**: 380-395. **DOI:** 10.1080/07055900.2011.623079

Trenberth KE, Dai A, Rasmussen RM, Parsons DB. 2003. The changing character of precipitation. *Bulletin of the American Meteorological Society* **84**: 1205-1217.

Ulbrich U, Brücher T, Fink AH, Leckebusch GC, Krüger A, Pinto JG. 2003. The central European floods of August 2002: Part 2 – Synoptic causes and considerations with respect to climate change. *Weather*, **58**, 434-442.

List of tables

Table 1. Station elevation, distances and beam height characteristics from the Strathmore weather radar.

List of figure captions

Figure 1. Map of southern Alberta showing the topography and locations of the precipitation stations in the Bow River sub-basin (black dots), and the Oldman River sub-basin (grey dots) examined in this study. The Calgary West CR10 auto (CWS), Burns Creek (BCR), Kananaskis (KAN), and Claresholm (CLA) precipitation stations are highlighted (large black dots); radar locations (Carvel (WHK) near Edmonton, Strathmore (XSM) near Calgary and Schuler (XBU) near Medicine Hat (black stars); and cities (Edmonton (YEG), Red Deer (YQF), Calgary (YYC), Lethbridge (YQL), and Medicine Hat (YXH) (red squares). The thick black outline represents the area of the Saskatchewan River Basin encompassing southern Alberta. The South Saskatchewan River flows through YQL, while the Bow, Red Deer and North Saskatchewan Rivers flow through YYC, YQF, and YEG, respectively. The Battle River is located between YEG and YQF.

Figure 2. Cloud to ground lightning flashes (upper panel) and vertical profiles of averaged reflectivity (lower panel) over (a) Burns Creek, (b) Calgary International and (c) Kananaskis Boundary auto stations from 0000 UTC June 18 to 0000 UTC June 23 2013. Heights are above ground level (AGL) at the radar. Reflectivity is indicated by the color bar to the right. Dotted lines in the lower panels are the rain-gauge cumulative rainfall accumulation in mm and solid lines are the hourly averaged rain-gauge estimated rainfall rates (scale to the right multiplied by 0.1) in mm h⁻¹.

Figure 3. Rainfall summaries for the stations analyzed in the a) Bow River sub-basin, and b) Oldman River sub-basin. The light and dark bars represent the total event rainfall and total thunderstorm rainfall, respectively. The red line represents the fraction of thunderstorm rainfall expressed as a percentage of the total rainfall. Stations are plotted from north to south.

Figure 4. The percentage contribution of thunderstorm rainfall to station total rainfall, stratified by CG lightning activity.

Figure 5. Reflectivity composites from the Silver Star Mountain (XSS), Carvel (WHK), Strathmore (XSM) and Schuler (XBU) radars at 1.5 km altitude above ground level on June 20 2013 at (a) 0300 UTC (b) 0500 UTC (c) 0800 UTC (d) 1500 UTC and (e) 2100 UTC. The Calgary West CR10 auto (CWS), Burns Creek (BCR), and Kananaskis (KAN) stations are underlined and marked with asterisks.

Figure 6. Mean radial wind field retrieved from Strathmore (XSM), plotted as a function of height and time, starting from 0000Z June 18 2013 and ending at 2300Z June 22 2013. The VAD winds are plotted at 3-hourly intervals.

Figure 7. Sequence of radar reflectivity cross-sections from XSM over Burns Creek (238° azimuth and 123 km range) from 0130-0500 UTC June 20 2013, in 30 minute intervals. Cross-sections are oriented along the 238° azimuth, starting at the radar and extending to 150 km. The altitude of BCR relative to the radar is indicated by the asterisk. Note XSM is east of BCR, so in these images east to west is from right to left.

Figure 8. The hydrometeor time series above Burns Creek, Alberta on 20 June 2013. The bold lines are the mixing ratio ($\text{kg}/\text{kg}_{\text{air}}$) of ice phase hydrometeor and the thin lines represent the liquid phase hydrometers. The mass content values of the liquid hydrometeors have been multiplied by 10. The bold black line indicates the 0°C level.

Figure 9. The vertical motion vertical field (Pa s^{-1}) at 0400 UTC and 0800 UTC, which corresponds to the convective and stratiform precipitation periods, respectively. The black bold line indicates the 0°C isotherm.

Figure 10. The difference between the height (km) of the freezing level (0°C line) and topography ($Z_{0\text{Cline}} - Z_{\text{topo}}$). The symbols show the location of Kananaskis (KAN), Burns Creek (BCR), Calgary (YYC) and the Strathmore radar (XSM).

Figure 11. Radar derived composite rainfall accumulation from 0000 UTC June 18 2013 to 2350 UTC June 22 2013, from Strathmore (XSM) and Schuler (XBU) radars. The Calgary West CR10 auto (CWS), Burns Creek (BCR), and Kananaskis (KAN) precipitation stations are highlighted (black dots).

Figure 12 Rainfall rates (upper panel) and rainfall accumulation (lower panel) for each of the selected locations (a) Burns Creek, (b) Calgary West, and (c) Kananaskis stations. Upper panels show radar-derived rainfall rates (thin dashed lines) using the Marshall-Palmer ZR relation. The solid lines in these panels are gauge hourly averaged rainfall rates. The lower panels of 12a, 12b, and 12c show the cumulative radar-derived rainfall accumulation (dashed line) and the cumulative gauge rainfall accumulation (solid line) for the event.

Figure 13. The total precipitation from the gauges within the Bow and Oldman catchment areas as a function of elevation.

Figure 14. The influence of topography on the evolution of rainfall intensity and CG flash activity, from 07 UTC June 19 to 06 UTC Jun 22, in 6-hrly time intervals.

Table 1. Station elevation, distances and beam height characteristics from the Strathmore weather radar.

	CWS	BCR	KAN
Station elevation (m ASL)	1081	1899	1464
Distance (km)	44	123	124
Beam height at 0.5° elevation scan above station (km)	0.35	1.50	1.50

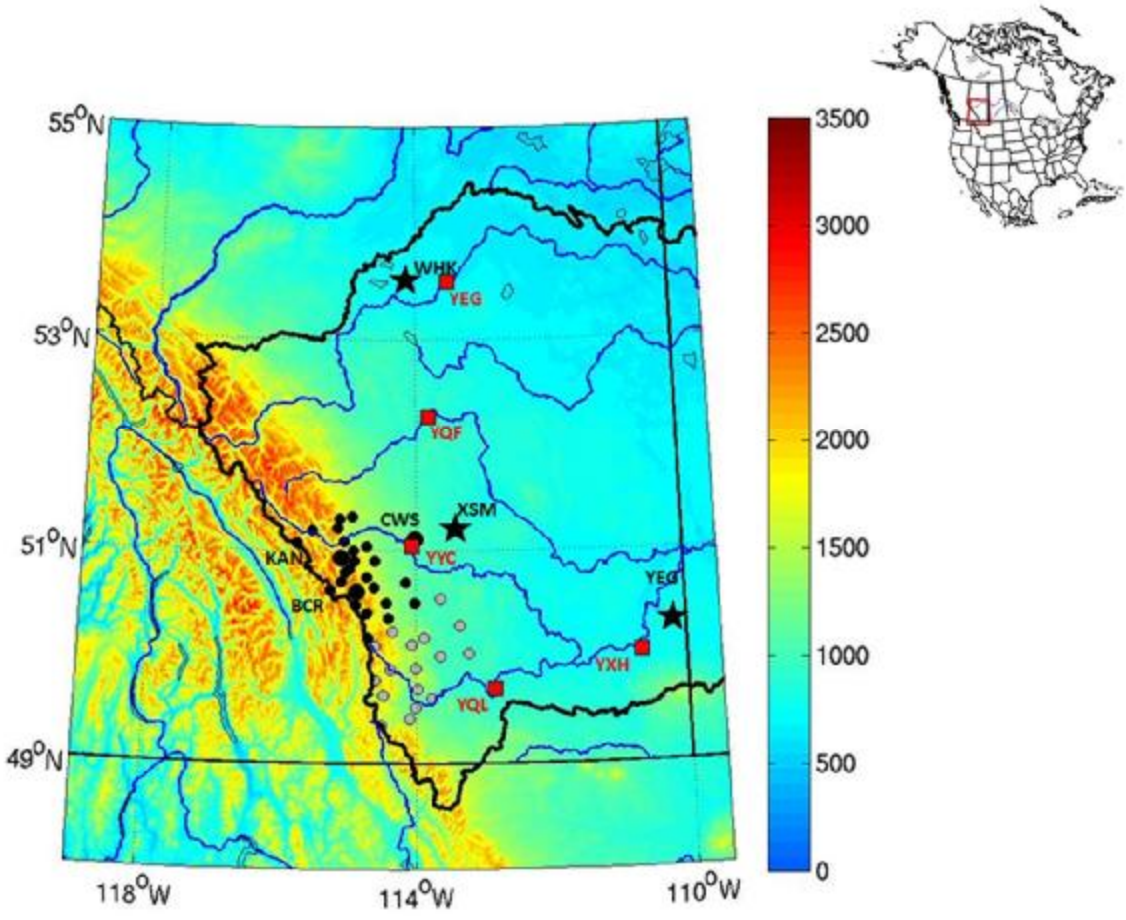


Figure 1.

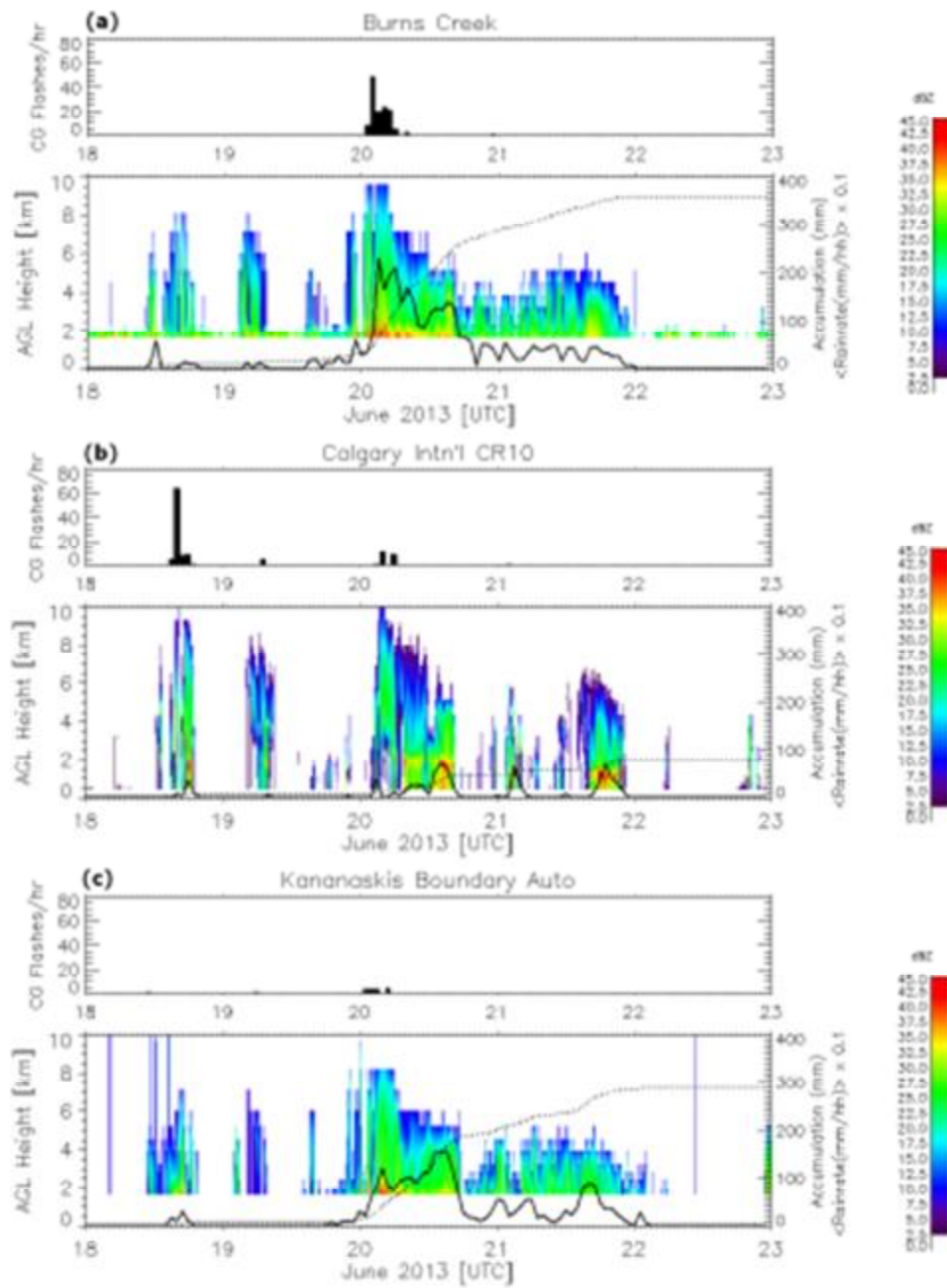


Figure 2.

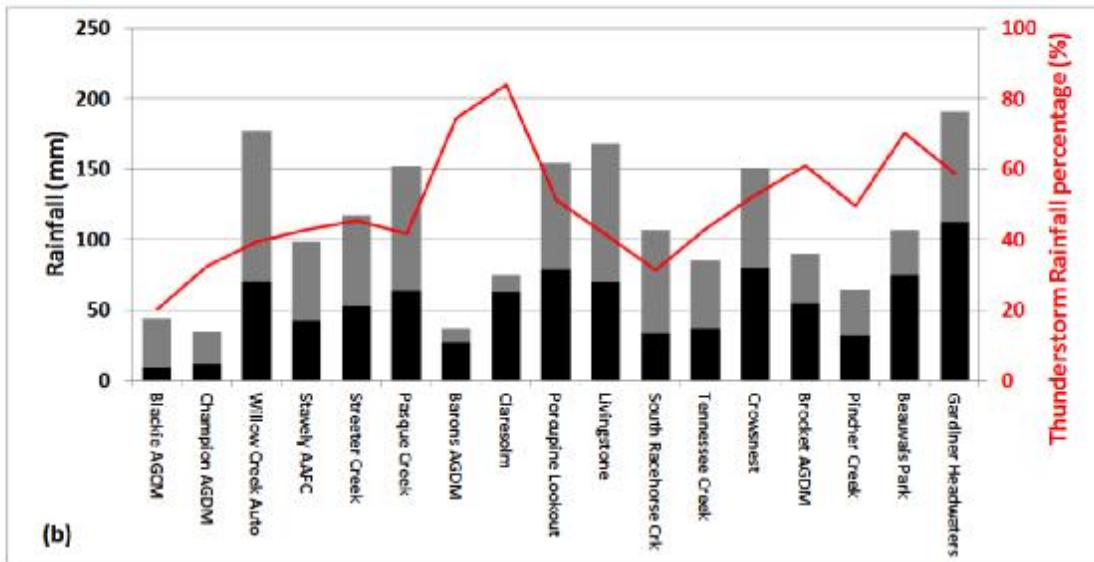
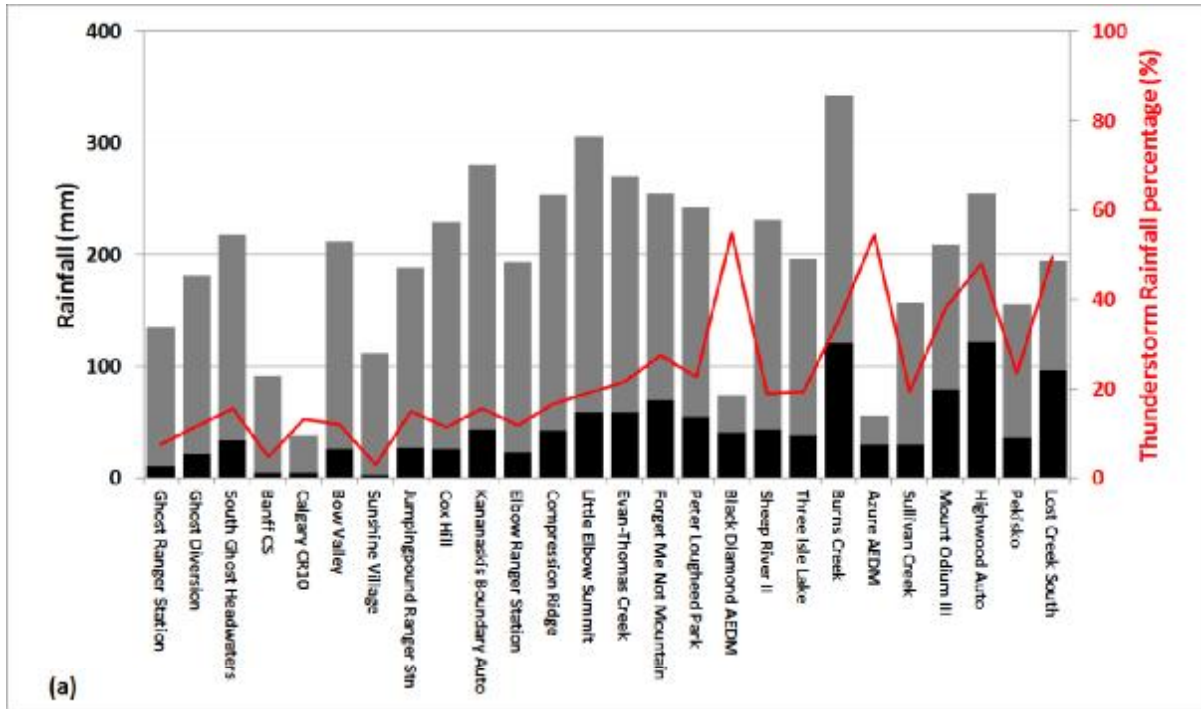


Figure 3.

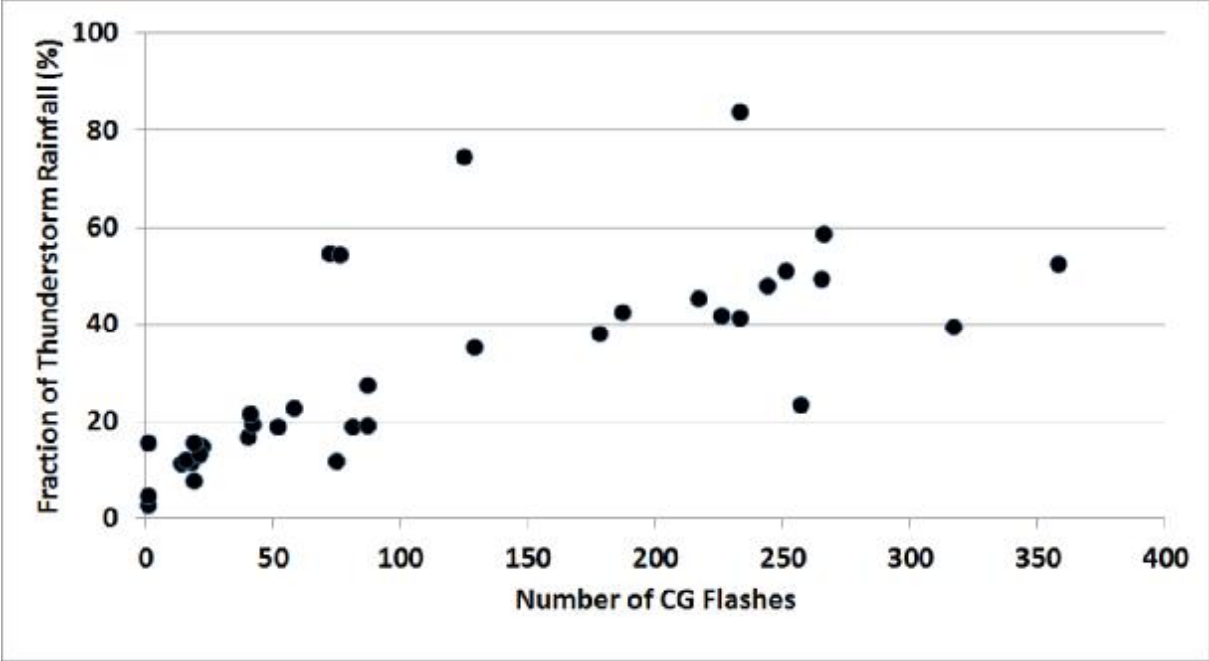


Figure 4.

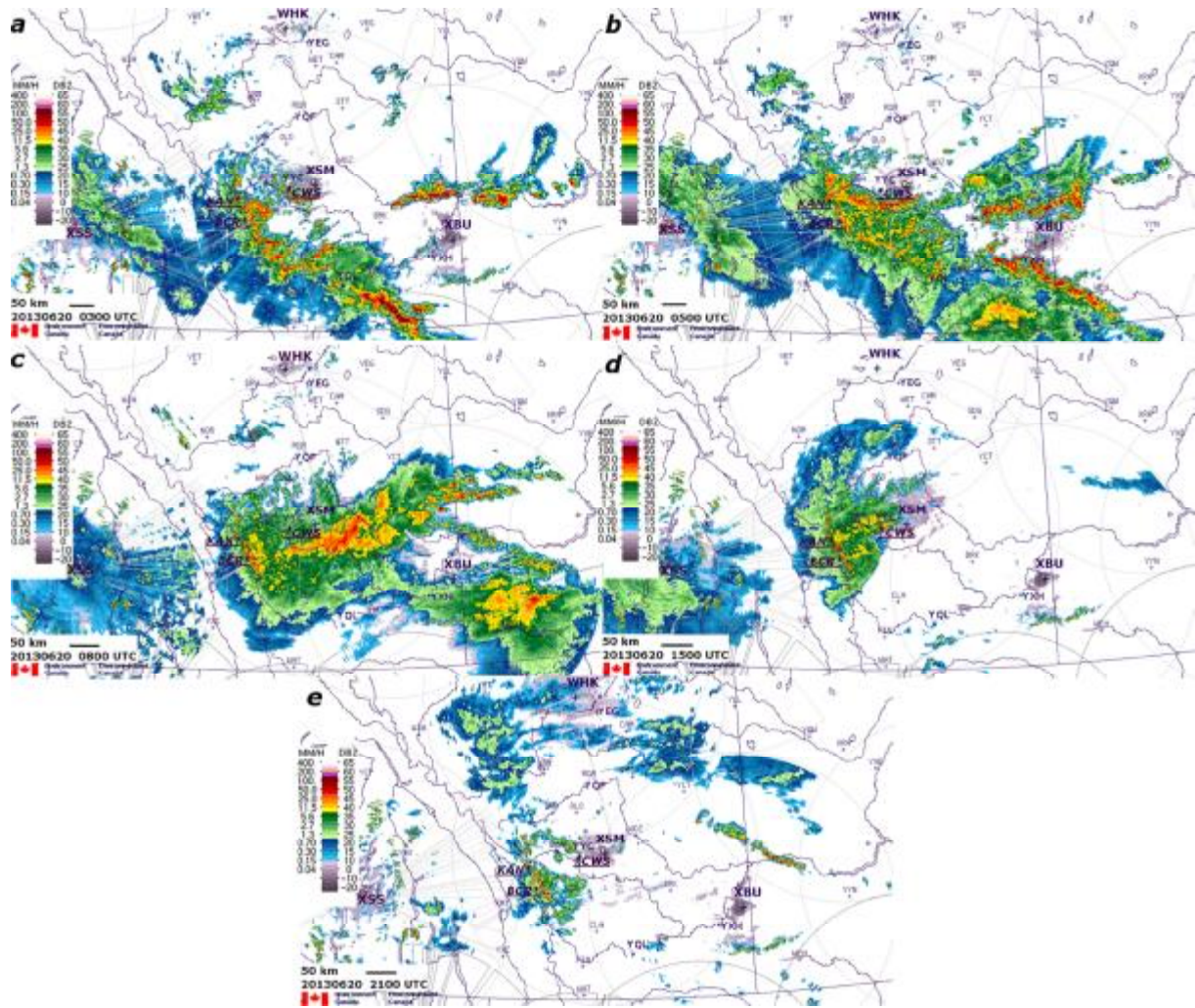


Figure 5.

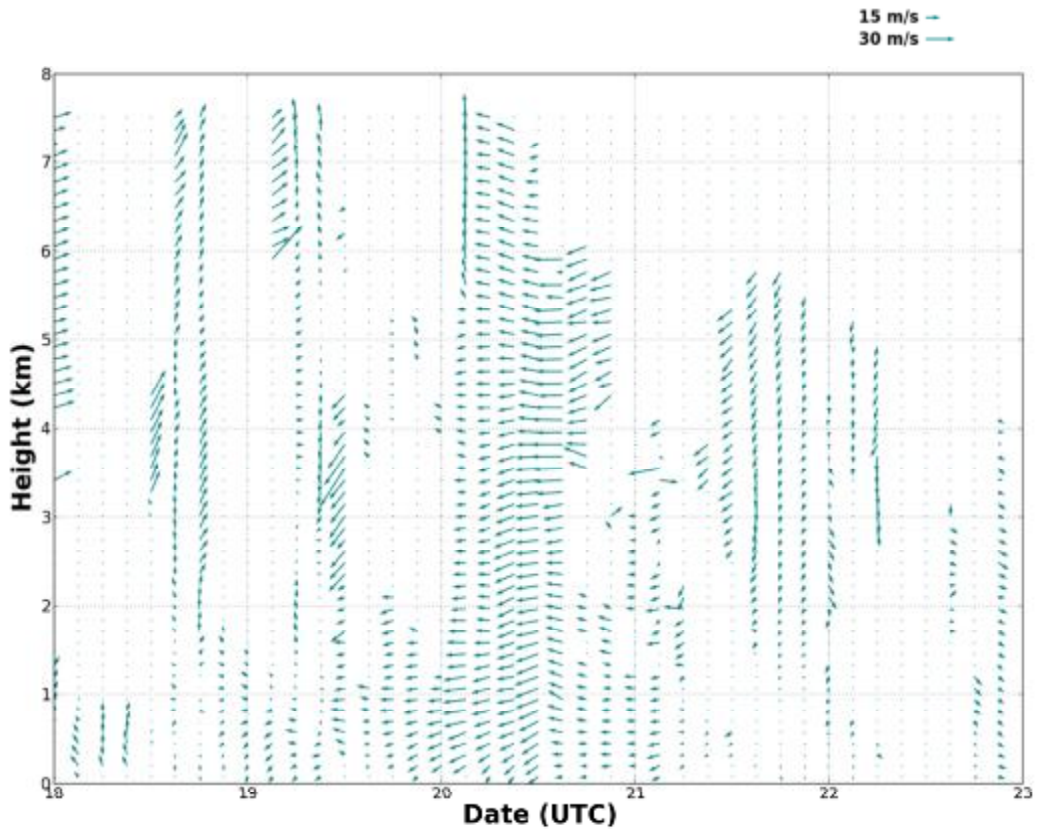


Figure 6.

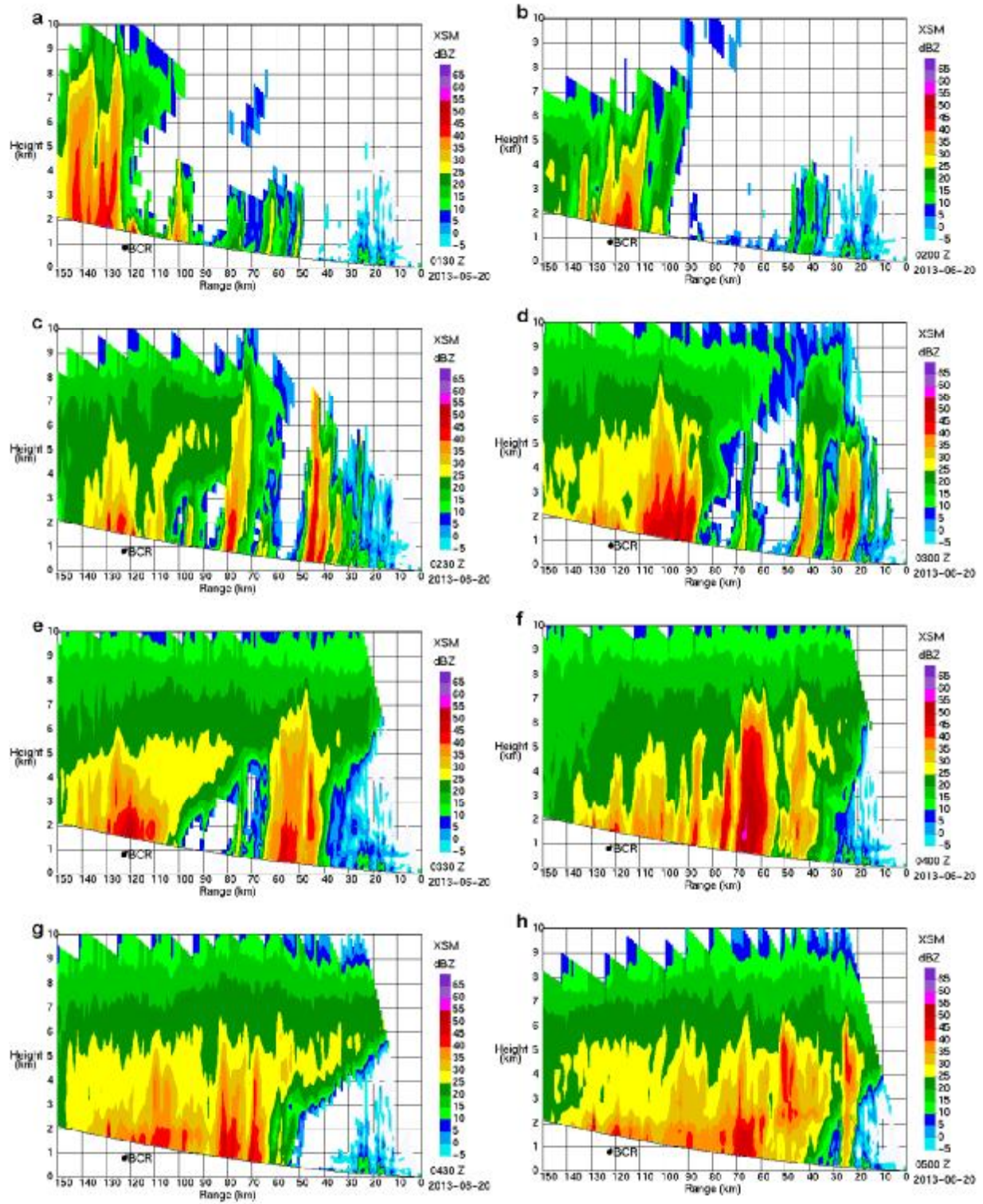


Figure 7.

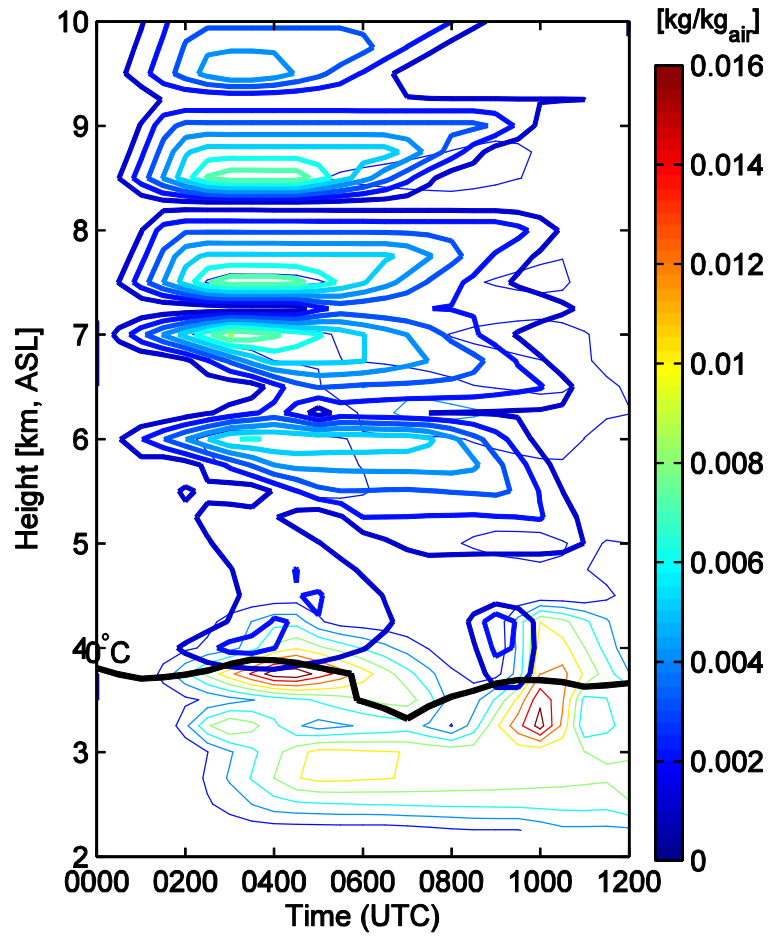


Figure 8.

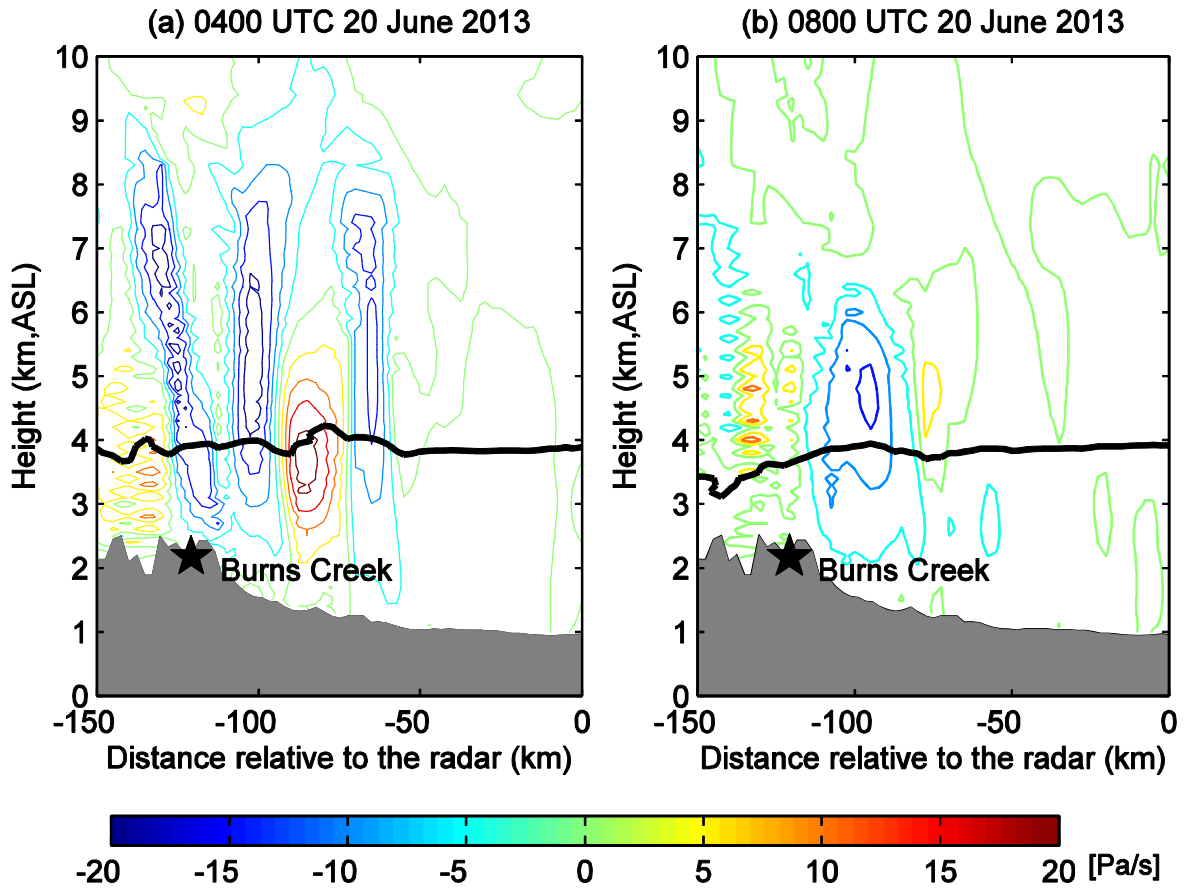


Figure 9.

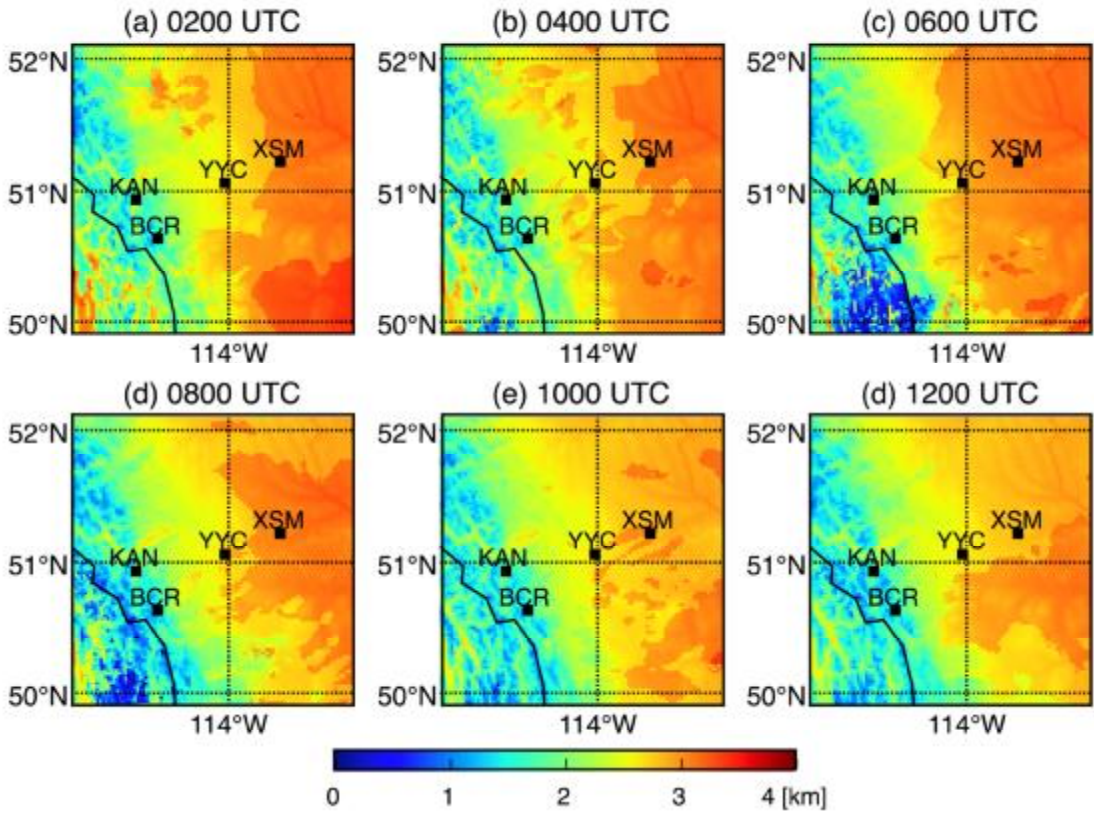


Figure 10.

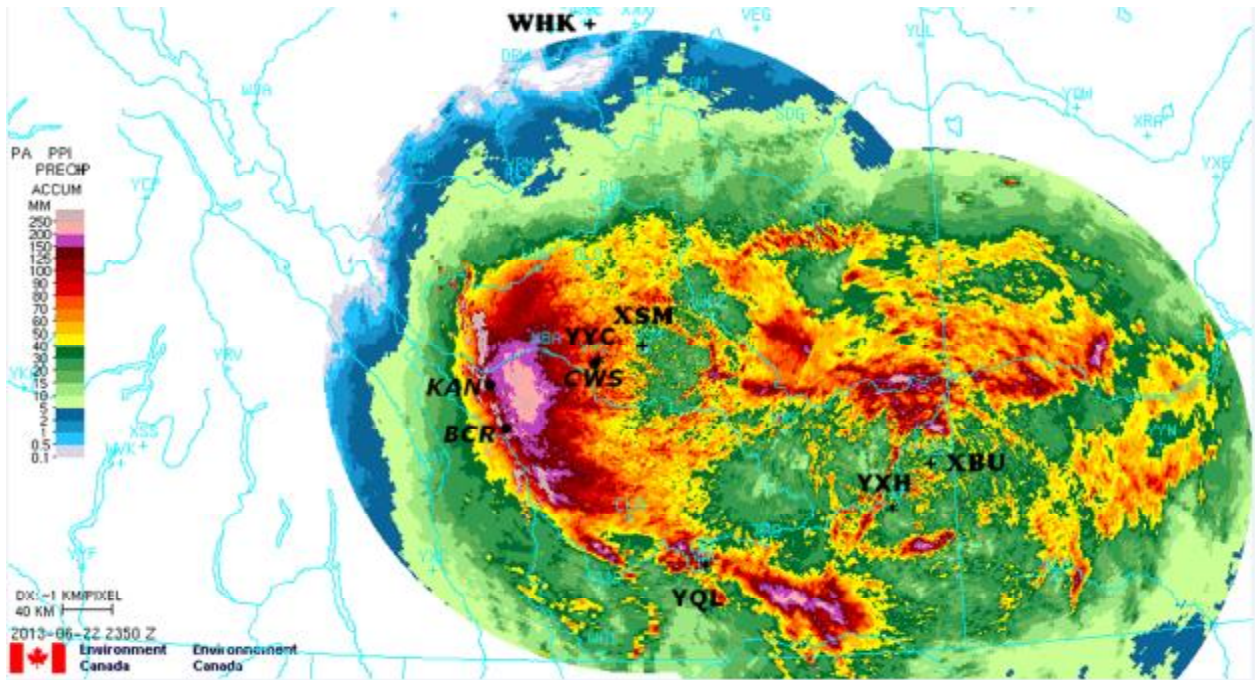


Figure 11.

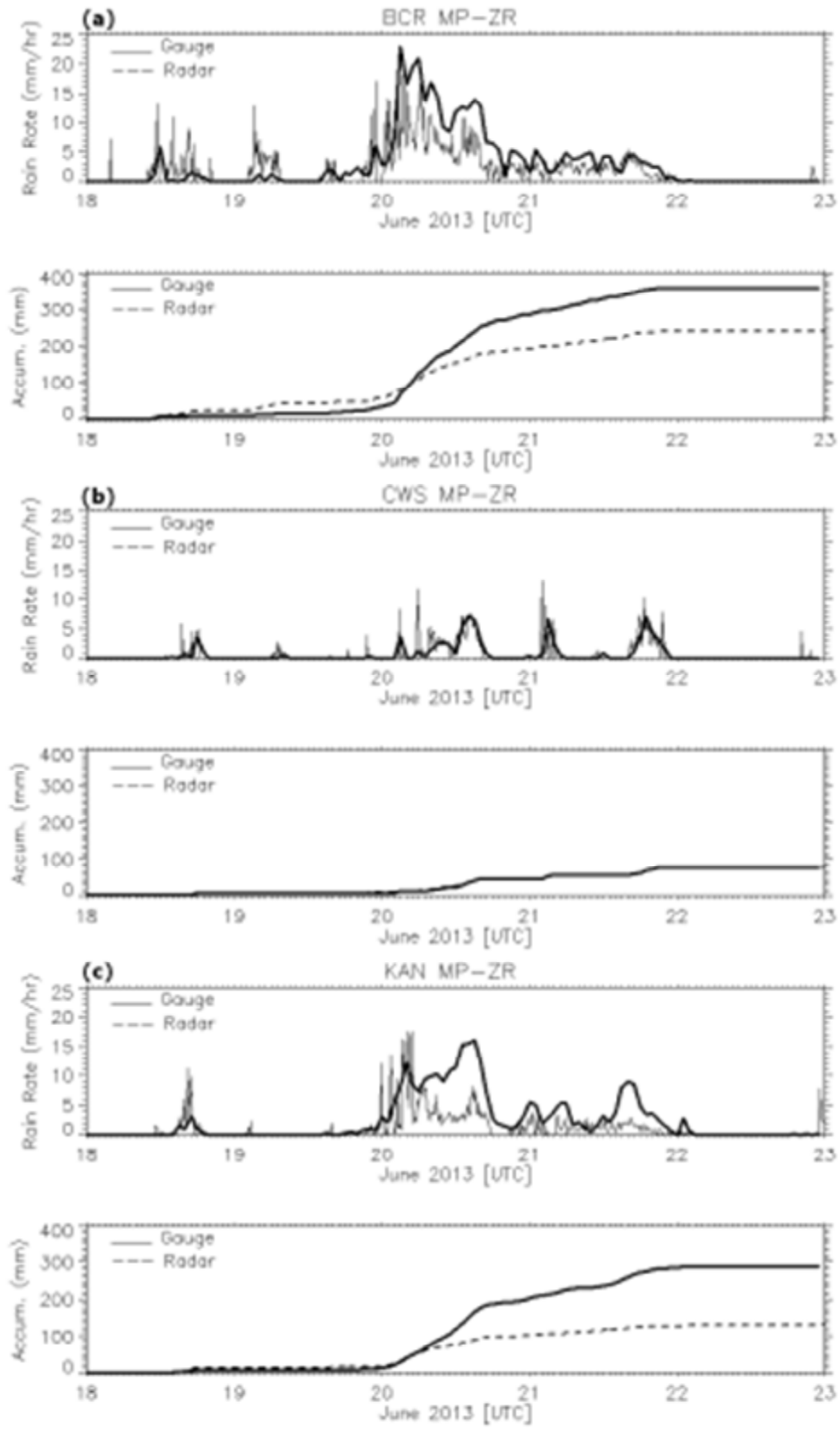


Figure 12.

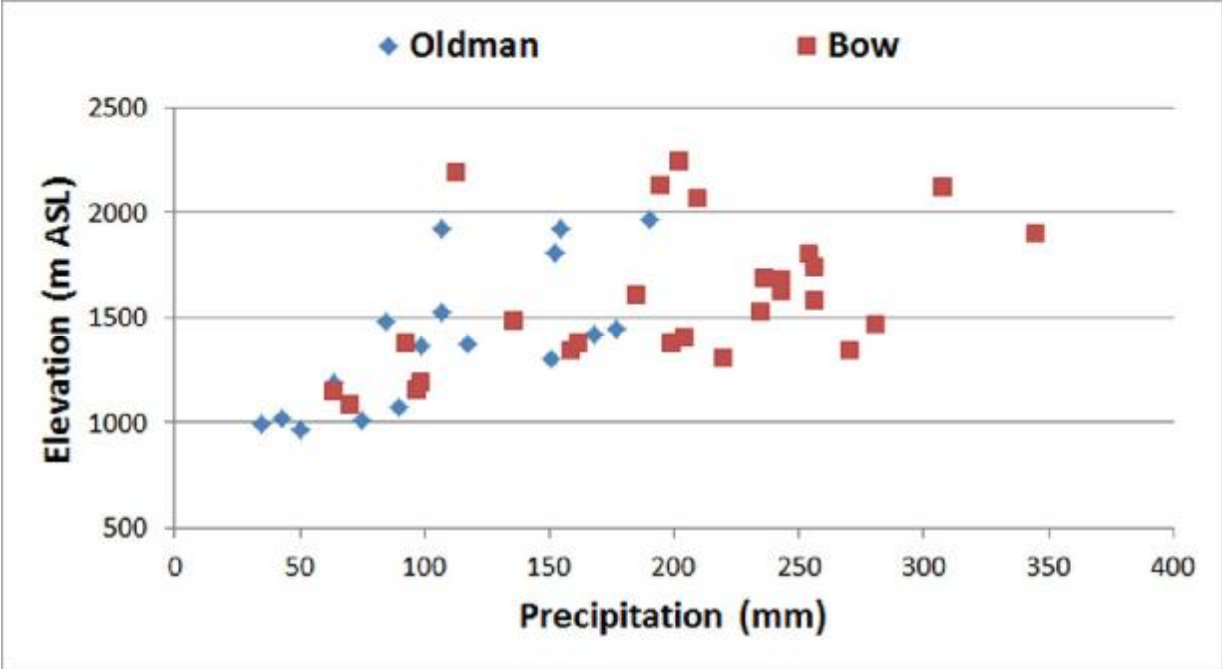


Figure 13.

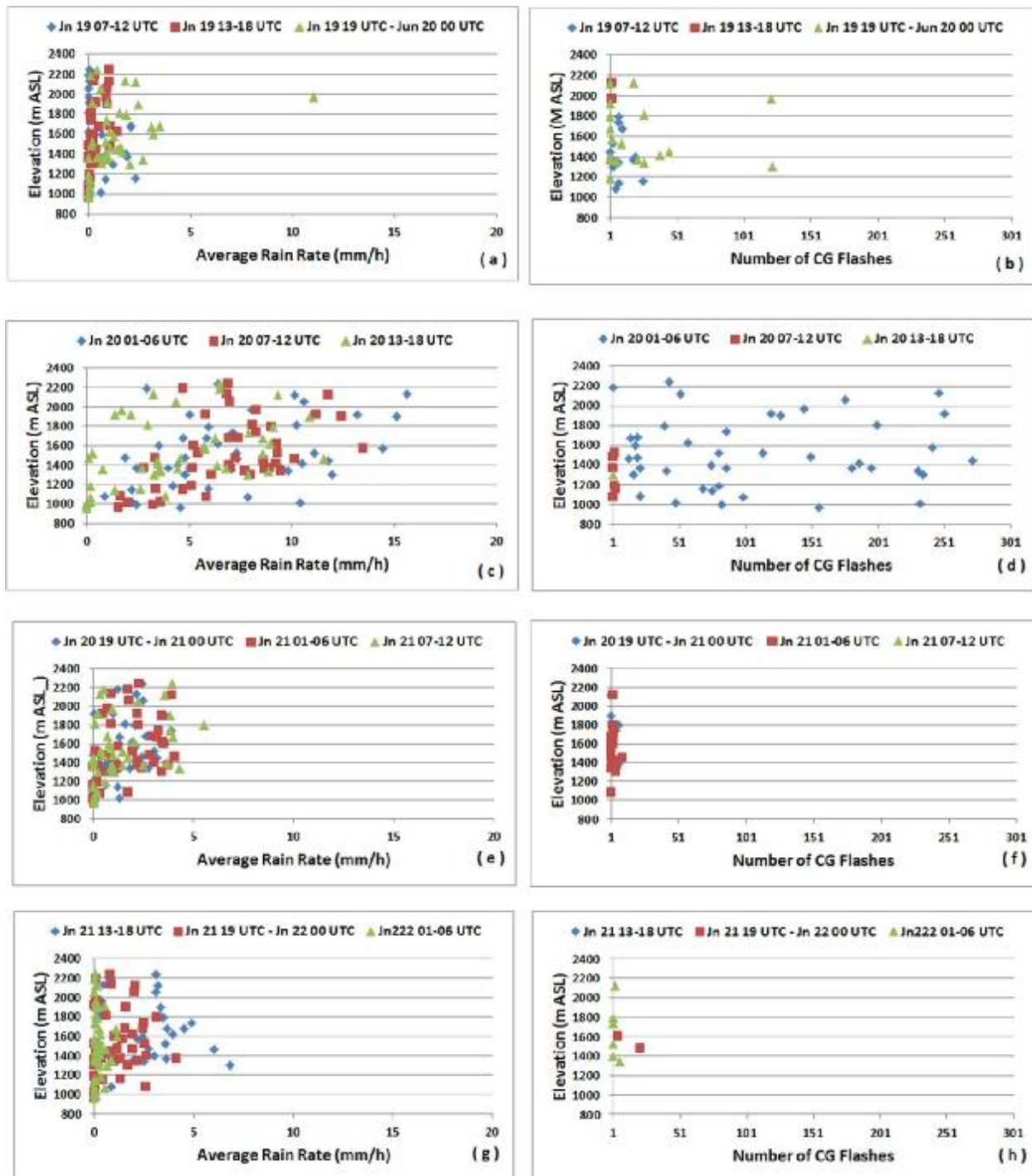


Figure 14.